PERGAMON

Solid-State Electronics 45 (2001) 1773–1785

SOLID-STATE ELECTRONICS

Modeling of time dependence of hole current and prediction of Q_{BD} and t_{BD} for thin gate MOS devices based upon anode hole injection

Mohammed T. Quddus [a,*], Thomas A. DeMassa [a], Dieter K. Schroder [a], Julian J. Sanchez [b]

[a] *Department of Electrical Engineering, Arizona State University, Tempe AZ 85287, USA*
[b] *Intel Corporation, 5000 W. Chandler Road, AZ 85224, USA*

Received 7 June 1999; received in revised form 10 May 2000

Abstract

A theoretical breakdown model based on anode hole injection is presented for evaluating the time dependence of injected electron and generated substrate hole current under constant voltage stress for thin gate oxide MOS devices. The model considers the effect of poly-depletion, quantum yield, first order trapping kinetics and different tunneling conditions for determining the time variation of hole current during constant voltage stress and correlates it to the buildup of the positive charge inside the oxide during the time dependent oxide breakdown process. The model is shown to agree well with the experimental results. Moreover, using the proposed model the intrinsic charge to breakdown Q_{BD} and the time to breakdown t_{BD} of thin gate oxide MOS devices can be satisfactorily predicted at different oxide voltages. © 2001 Elsevier Science Ltd. All rights reserved.

Keywords: Poly-depletion; Quantum yield; Charge to breakdown; Time to breakdown; Hole generation efficiency

1. Introduction

One of the on going trends of scaling down the supply voltage in VLSI technology is driven by goals to reduce the power consumption, maintain sufficient circuit reliability and optimize circuit performance in the presence of ever increasing circuit densities. But the reduction in supply voltage will definitely result in a reduction in speed unless the thickness of the gate oxide is scaled accordingly. The gate oxide thickness is reduced aggressively in order to compensate for the drop in speed at low voltages for digital applications. However, the presence of high electric fields across the gate oxide due to scaling impose a serious reliability problem and hence causes the premature breakdown of the oxide which is identified as one of the major failure mechanisms for MOS-VLSI integrated circuits.

It is believed by most researchers [1–3] that the time dependent dielectric breakdown in thin oxides is triggered due to the buildup of the positive charge when local hole trapping occurs near the hole charge trapped interface during F–N tunneling of electrons. The field at the localized trapped area reaches a critical value which causes the breakdown of the oxide. The charge to breakdown Q_{BD} which measures the breakdown strength is determined by the charge injected during the buildup stage and the time required for the buildup of the charge determines the lifetime t_{BD} of the oxide.

Data supporting the substrate hole induced breakdown mechanism lies in the generation of holes and its role in the buildup of the positive charge during the high field F–N stress. The charge to breakdown Q_{BD} is essentially linked to the hole generation current and hence

* Corresponding author. Address: On Semiconductor, 5005 East McDowell Road Malldrop-D145, Phoenix, AZ 85008, USA. Tel.: +1-620-244-4437; fax: +1-602-244-6008.

E-mail address: tanvir.quddus@onsemi.com (M.T. Quddus).

0038-1101/01/$ - see front matter © 2001 Elsevier Science Ltd. All rights reserved.
PII: S0038-1101(01)00199-X

generation efficiency [4,5]. There are several possible mechanisms that can give rise to the generation of hole current. Hole generation is initiated by the energetic electrons and the energy gained by these electrons during their passage through the oxide will determine which mechanism will be responsible for the generation of hole as different mechanisms have different threshold energy for hole generation. For thicker oxides the hole generation is dominated by the bandgap impact ionization when the operating voltage is larger than the bandgap energy (9 eV) of SiO_2 [1,2]. However for thin oxides, the bandgap impact ionization cannot be the main mechanism responsible for the generation of holes as the energy acquired by the electrons during its transport through the oxide is less than the threshold energy of the bandgap impact ionization in SiO_2. Among different possible origins [4] of substrate hole current, the hole current due to hole injection from the anode due to either surface plasmons [6–9] or direct excitation [10,11] mechanisms is considered to be the most prevalent one [3,12] because of the dependence of hole current on anode material [6,13–15]. In this paper a hole induced breakdown model based on anode hole injection is presented to determine the intrinsic (defect free oxides) [3] charge to breakdown Q_{BD} and time to breakdown t_{BD} for thin oxides. The proposed model considers the poly-depletion effect and quantum yield in Si to calculate the hole generation efficiency for different oxide voltages. Moreover, the time dependence of injected electron and generated hole current is modeled considering the effect of first order trapping kinetics and different tunneling conditions for both electrons injected from the cathode and holes generated from the anode.

2. Anode hole injection and charge to breakdown Q_{BD} model

The proposed anode hole injection model is illustrated with the help of the energy band diagram as shown in Fig. 1. At sufficiently large dielectric fields, the injected electrons from the conduction band of the cathode will travel through the oxide and will gain an energy E_n during their transport through the oxide. A significant fraction of these incident tunneling electrons (J_n) will lose their energy E_{ne} to a deep valence band electron after arriving at the anode. This release of energy by the energetic electrons will lift the valence band electrons to the lowest available energy state of the conduction band at the anode leaving behind hot holes. A small fraction of these holes will eventually tunnel back into the oxide. Some part of these tunneled holes will be able to reach the cathode giving rise to the hole current J_p and some of them will be trapped in localized areas inside the oxide. Hole traps are thought to be caused by oxygen vacancies in the bulk and/or dangling bonds at the surface. Location with such a propensity to trap positive charge are postulated to make up only $\sim 10^{-6}$ of the total oxide area [2].

Fig. 1. Energy band diagram showing the anode hole injection process during F–N tunneling for a trap free oxide.

The locally trapped holes inside the oxide increase the positive charge and hence the field at the injecting interface. This process continues with the applied stress time in a positive feedback fashion, damaging the oxide and causing the tunneling current to increase in these locations. When the density of the localized trapped charge reaches some critical value Q_{ot}, the local electron tunneling current is increased to the point where the oxide breaks down. At the time of breakdown, the hole fluence to breakdown is also expected to reach a constant value [4]. Accordingly, the charge to breakdown Q_{BD} can be related to Q_P by

$$Q_{BD} = Q_P\left(\frac{J_n}{J_p}\right) \tag{1}$$

where

$$Q_{BD} = \int_0^{t_{BD}} J_n(t)\,dt \cong J_n t_{BD} \tag{2}$$

$$Q_P = \int_0^{t_{BD}} J_p(t)\,dt \cong J_p t_{BD} \tag{3}$$

In order to model the hole generation current J_p, it is necessary to calculate the average electron energy E_{ne} as electrons reach the anode. In the context of hole injection from the anode (Fig. 1), it is obvious that a higher voltage across the gate oxide (i.e. higher gate electric

field) will provide more energy to the electron reaching the anode and a lower barrier height for the tunneling of holes into the oxide from the anode side. Therefore, with a higher gate oxide voltage V_{ox}, the injection current density due to holes from the anode will be higher and hence the probability of damage at the substrate oxide interface is much larger. The computation of average electron energy E_{ne}, while passing through the oxide, makes it necessary to relate the oxide voltage V_{ox} to the applied gate voltage V_g.

2.1. Oxide voltage V_{ox}

Accurate computation of the oxide voltage V_{ox} for a positive gate voltage V_g applied to the n^+ gate with p-type substrate (n^+p structure) requires accounting for the voltage drop across the poly-gate due to the poly-depletion effect [16,17]. The Medici device simulator is used to find the oxide voltage V_{ox}, when positive gate voltage V_g is applied to a n^+p MOS structure. The simulated distribution of potential across the poly-gate, oxide and substrate at different gate voltages clearly indicates the presence of significant poly-voltage V_{poly} across the gate at higher gate voltages [18] for the achievable maximum poly-doping concentration (5×10^{19} cm^{-3}) in thin oxides [3]. Also, the flat band voltage V_{FB} and semiconductor voltage V_{semi} almost cancel each other and hence the correction factor $K(|V_g| - |V_{ox}|)$ nearly follows the variation of V_{poly} with gate bias V_g. The correction factor K can be modeled [19] using the theoretical expression of poly-voltage under the depletion approximation which can be obtained by solving the continuity equation and applying Gauss's law at the poly-oxide interface and is given by [20–22]

$$V_{poly} = \frac{E_{ox}^2 \varepsilon_{ox}^2}{2\varepsilon_{Si} q N_{poly}} \quad (4)$$

The expression for correction factor K finally becomes

$$K = K' + V_{FB} + V_{semi} = |V_g| - |V_{ox}| \quad (5)$$

where

$$K' = V_{poly} = \frac{1}{2m}\left[2mV_g' + 1 - \sqrt{1 + 4mV_g'}\right] \quad (6)$$

and

$$m = \frac{\varepsilon_{ox}^2}{2\varepsilon_{Si} q}\left[\frac{1}{N_{poly}}\right]\frac{1}{t_{ox}^2} \quad (7)$$

Fig. 2 shows the variation of correction factor K with positive gate voltage V_g for different oxide thicknesses and a poly-doping of 5×10^{19} cm^{-3}. As shown in Fig. 2 values of correction factor K obtained from Eq. (5) for different oxide thickness matches closely with that of the Medici simulated results. For a negative gate voltage V_g applied to the n^+ gate with p-type substrate, both poly-gate and Si substrate are in accumulation. The results obtained from the Medici simulation shows that the correction factor K for such a case is independent of poly-doping as well as oxide thickness but depends on gate voltage [18]. The simulated quasi-static C–V curves shown in Fig. 3 also shows the effect of poly-depletion (reduced gate capacitance in the strong Si inversion regime) for different oxide thickness and a poly-doping of

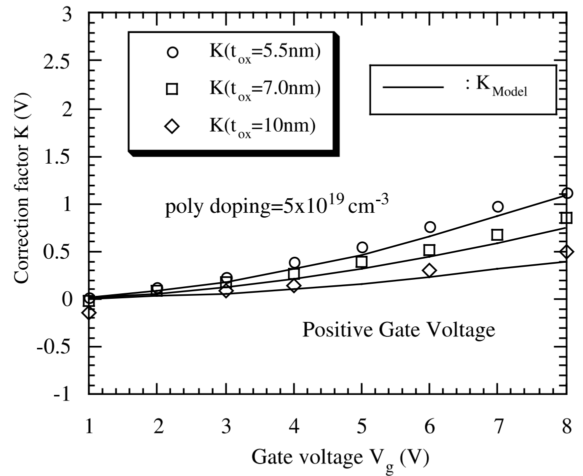

Fig. 2. Variation of correction factor K of a n^+p structure as a function of positive gate voltage V_g for different oxide thicknesses and poly-doping of 5×10^{19} cm^{-3}. Medici simulated results are represented by symbols.

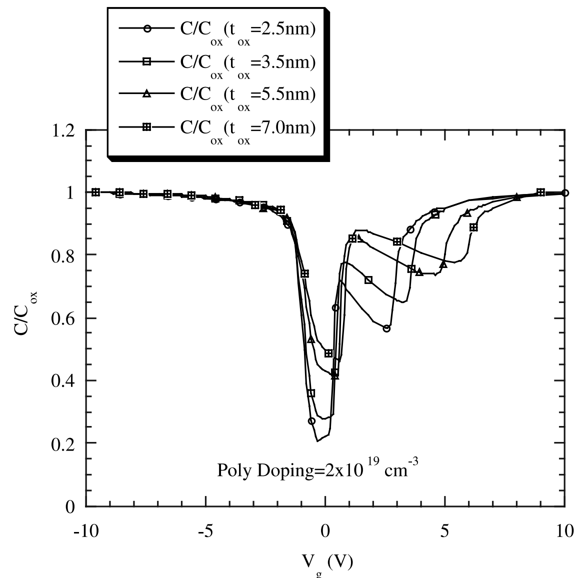

Fig. 3. Medici simulated quasi-static C–V curves showing the effect of poly-depletion (reduced gate capacitance in inversion) for different oxide thicknesses and a poly-doping of 2×10^{19} cm^{-3}.

Table 1
Correction factor K for different poly-gate and substrate types

Poly-gate and substrate type	Polarity of gate bias	Correction factor K[a]
n^+ poly on p-substrate	$+V_g$	$K' = \frac{1}{2m}\left(2mV'_g + 1 - \sqrt{1+4mV'_g}\right)$
n^+ poly on p-substrate	$-V_g$	$K = 1.01 + 0.35\lvert V_g\rvert$
p^+ poly on n-substrate	$+V_g$	$K = 1.01 + 0.35\,V_g$
p^+ poly on n-substrate	$-V_g$	$\lvert K'\rvert = \frac{1}{2m}\left(2m\lvert V'_g\rvert + 1 - \sqrt{1+4m\lvert V'_g\rvert}\right)$

[a] $K = \lvert K' + V_{FB} + V_{semi}\rvert = \lvert V_g\rvert - \lvert V_{ox}\rvert$ ($m = \frac{\varepsilon_{ox}^2}{2\varepsilon_{Si}q}\left[\frac{1}{N_{poly}}\right]\frac{1}{t_{ox}^2}$ and $V'_g = V_g - V_{FB} - V_{semi}$).

2×10^{19} cm^{-3}, which is similar to the result as reported earlier [16,17]. Moreover, the onset of recovery point (poly becomes inverted) shifts toward higher gate voltage for larger thickness. The effect of poly-depletion is significant for a poly-doping less than 5×10^{19} cm^{-3} and an oxide thickness less than $\approx$12 nm. The correction factor K in general, for different substrate and poly-doping, is summarized in Table 1.

2.2. Average electron energy E_{ne}

In very thin oxides at oxide voltage $V_{ox} < \Phi_B$, the electron tunneling is dominated by direct tunneling and the electrons do not experience scattering in traversing the oxide. Hence, the transport of electrons through the oxide is nearly ballistic [23].

The arrival energy of the electron E_{ne} (energy with respect to anode conduction band) at the anode for direct tunneling is simply

$$E_{ne} = qV_{ox} \quad \text{for} \quad V_{ox} < \Phi_B \tag{8}$$

In the F–N tunneling region ($V_{ox} > \Phi_B$), electrons gain KE from the applied oxide field on one hand and do suffer scattering due to phonon or other possible inelastic scattering on the other hand. The average energy in the F–N tunneling region can still be obtained from the phenomenological equation [23] using an energy dependent relaxation length λ in the equation. In most of the well established models [3,4], the value of λ is assumed a constant as a first order of approximation which is not true. In this paper a polynomial function is used to get the similar variation of λ with electron energy E_n (energy with respect to oxide conduction band) as described in Ref. [9] for the calculation of average energy E_{ne}. The phenomenological equation [23] used in our model for the calculation of the average energy E_{ne} can be written as

$$\frac{dE_n(x)}{dx} = -qE_{ox}(x) - \frac{E_n(x)}{\lambda(E_n)} \quad \text{for} \quad V_{ox} > \Phi_B \tag{9}$$

The relationship between E_n and λ in Eq. (9) is described by the following polynomial function

$$\lambda(E_n) = a_0 + a_1E_n + a_2E_n^2 + a_3E_n^3 + a_4E_n^4 \tag{10}$$

where $a_0 = 0.19974$, $a_1 = 8.6295$, $a_2 = -3.3119$, $a_3 = 0.4409$, $a_4 = -0.021128$.

By solving Eq. (9) numerically for $E_n(x)$ at $x = t_{ox} - x_t$ the average energy of electrons reaching the anode can be represented by

$$E_{ne} = q\Phi_B + E_n(x = t_{ox} - x_t) \tag{11}$$

The average energy E_{ne} of an electron (as it travels from cathode to anode) obtained using our model equations (9)–(11) is in good agreement with the Monte Carlo simulation [24] as shown in Fig. 4(a). The model is valid for an oxide thickness of 4.0–13.0 nm and an average electron energy of 0–8.5 eV.

2.3. Hole generation efficiency J_p/J_n

The energetic electrons reaching the anode will liberate energy E_{ne} to create hot holes with energy E_{np}. Only a fraction of the generated holes with proper momentum for tunneling from the anode will be able to reach the cathode to generate hole current J_p. The number of electron/hot hole pairs generated by incident electron will be determined by the quantum yield γ in poly-Si [9,23]. Accordingly, the energy of a hot hole is given by

$$E_{np} = \frac{E_{ne}}{\gamma} \tag{12}$$

Hence, the barrier height Φ_p for hot holes tunneling into the oxide from the anode side is given by

$$q\Phi_p = E_{G,SiO_2} - q\Phi_B - \frac{E_{ne}}{\gamma} \tag{13}$$

Mathematically, the hole tunneling current density J_p is given as [9,25]

$$J_p = \alpha_p J_n \gamma T_p \tag{14}$$

where α_p is the hole generation coefficient and T_p is the hole tunneling probability for a trap free oxide (i.e. $t = 0$) and is given by the WKB formula [15]

$$T_p = \exp\left[-\frac{C}{E_{ox}}(\Phi_p)^{3/2}\right] \tag{15}$$

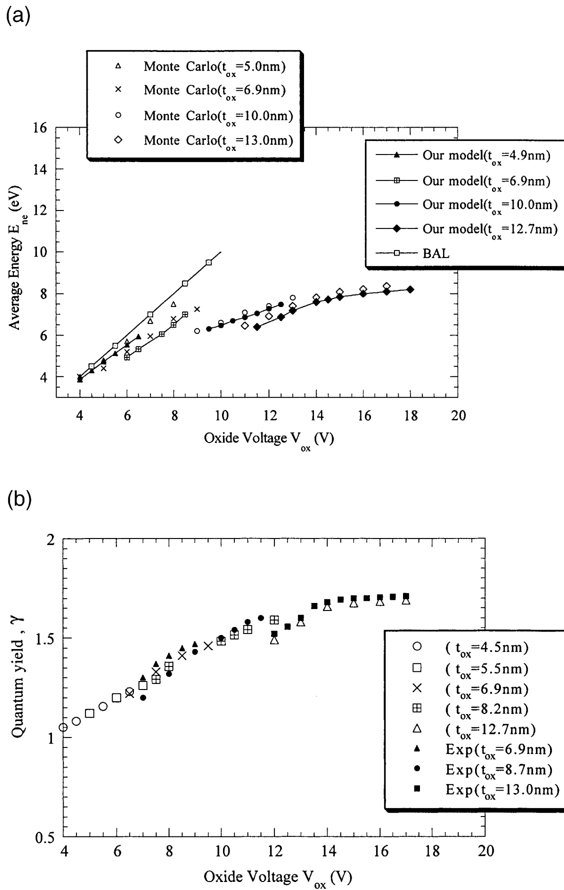

Fig. 4. (a) Average electron energy E_{ne} as a function of oxide (SiO_2) voltage V_{ox} obtained from our model and than that of Monte Carlo simulation [24]. The condition for ballistic transport ($E_{ne} = V_{ox}$) is indicated by BAL in the inset. Reprinted with permission from Ref. [24]. (© 1996 American Institute of Physics). (b) Comparison of experimentally measured γ values [23,26] and those deduced from our breakdown model as a fitting parameter. Solid symbols represent the experimentally measured γ data and the rest of the symbols represent the data obtained from our model. Reprinted with permission from Refs. [23,26]. (© 1985, 1995 American Institute of Physics).

where $C = (8\pi/3h)\sqrt{2m_{oxp}q}$, h is the Planck constant and m_{oxp} is the hole effective mass.

Fig. 4(b) shows the variation of γ with oxide voltage V_{ox} determined by the fitting equation and also those measured experimentally [23,26]. Fig. 4(b) shows the consistency between γ vs V_{ox} data predicted from our model and the previously published experimental γ data. At voltages less than 6–7 V the value of quantum yield γ is almost independent of oxide thickness and depends only on oxide voltage V_{ox} for thinner oxides [23] as its travel through the oxide is nearly ballistic [24]. However, on the contrary at a voltage higher than 6 V or so, the value of γ becomes thickness dependent for thicker oxides [23]. This is due to significant deviation of electron transport from ballistic one because of its scattering with oxide phonons. The parameter $J_n\gamma$ represents the generated hot hole at the anode and the hole coefficient α_p takes into account those generated holes which retain the appropriate momentum and energy for tunneling into the oxide. A value of 0.075 is taken for α_p as a fitting constant for our model.

3. Breakdown lifetime t_{BD} model

For thinner oxides with negligible carrier trapping inside the oxide, the injected current density J_n is almost constant with time t [25]. Hence, using expression (2) the time to breakdown t_{BD} can be related to J_n by $t_{BD} = Q_{BD}/J_n$. However, for relatively thicker oxides the effect of trapping cannot be neglected and the stressing current density J_n varies more than one or two orders of magnitude [20,25] depending on the stress time. Therefore, the actual time to breakdown t_{BD} for these oxides can only be obtained from the $t_{BD} = Q_{BD}/J_n$ expression when J_n is replaced with $J_{nave}(t_{BD})$, where $J_{nave}(t_{BD})$ is the log average of the initial current density $J_n(0)$ and current density just prior to breakdown $J_n(t_{BD})$. $J_{nave}(t_{BD})$ is given by

$$J_{nave}(t_{BD}) = 10^{[\log J_n(0) + \log J_n(t_{BD})]/2}$$

4. Model for $J_n(t)$ and $J_p(t)$

The breakdown in thin oxides is a time dependent process which can be split in two steps. During the first step (buildup stage), the oxide is slowly degraded due to the formation of localized high field/current density regions as a result of the trapping of both electrons and holes inside the oxide under electrical stress. When the localized field/current density reaches a critical value, the brief and rapid second step (runway) begins, during which thermal and/or electrical runway quickly brings the oxide to destructive breakdown by forming a permanent conductive path between gate and substrate. The time required to complete the buildup stage determines the lifetime (t_{BD}) and the charge injected during the buildup stage determines the breakdown strength (Q_{BD}). The eventual formation of localized high field or current density region is believed to be due to the accumulation of positive charges near the cathode in localized areas. Though several different possible mechanisms of positive charge generation [27] have been reported in the literature, generation of hole current and hence positive charge due to hole injection from the anode and its subsequent trapping inside the oxide is considered as the most promising one in thin oxides.

Therefore, the model proposed here for determining the time dependence of hole current density $J_p(t)$ is based on hole injection from the anode and its trapping in a localized area near the cathode. The model also inherently predicts the time dependence of injected current density $J_n(t)$. Though hole trapping is considered as the precursor of oxide breakdown, the effect of electron trapping on the distribution of internal electric fields cannot be neglected as both $J_p(t)$ and $J_n(t)$ will be determined by the internal field inside the oxide. The latter quantity is then used in determining the breakdown lifetime t_{BD} of thin oxides.

Following the previously suggested theory [2], the total oxide area in our model has been divided into two which are connected in parallel. One of them is localized weak area A_l, with trapped holes and electrons and the other one is a robust area A_r with only trapped electrons. The robust area A_r is much larger in size than weak area A_l. Fig. 5(a) shows the energy band diagram representing a sheet of positive charge Q^+ and a sheet of negative charge Q^- in the weak region of area A_l with hole and electron trapping at their respective centroids of x^+ and x^-. Fig. 5(b) shows the energy band diagram corresponding to a sheet of negative charge Q^- located at its centroid x^- due to bulk electron trapping in the robust region of area A_r. Therefore, the expressions for total electron and hole current density $J_n(t)$ and $J_p(t)$ are given by

$$J_n(t) = \frac{J_{nl}(t)A_l + J_{nr}(t)A_r}{A_l + A_r} \tag{16a}$$

$$J_p(t) = \frac{J_{pl}(t)A_l + J_{pr}(t)A_r}{A_l + A_r} \tag{16b}$$

where J_{nl} and J_{pl} represents the electron and hole current density in a localized area. The corresponding hole and electron current density in the robust area is represented by J_{nr} and J_{pr}.

4.1. Local area currents $J_{nl}(t)$ and $J_{pl}(t)$

Charge trapping inside the oxide results in distortion of the electric field. The energy band diagram corresponding to the local oxide area is shown in Fig. 5(a). Referring to Fig. 5(a) and using Gauss's law the cathode field E_{cl}, the mid region (between x^+ and x^-) field E_{ml} and the anode field E_{al} in the local area can be obtained as

$$\begin{aligned} E_{cl} &= \frac{V_{ox}}{x^+} - \frac{E_{ml}(x^- - x^+)}{x^+} - \frac{E_{al}(t_{ox} - x^-)}{x^+} \\ &= \frac{1}{x^+}[V_{ox} - E_{ml}(x^- - x^+) - E_{al}(t_{ox} - x^-)] \end{aligned} \tag{17a}$$

$$E_{ml} = E_{cl} - \frac{Q^+}{\varepsilon_{ox}} \tag{17b}$$

$$E_{al} = E_{ml} + \frac{Q^-}{\varepsilon_{ox}} \tag{17c}$$

where ε_{ox} is the permittivity of oxide and V_{ox} is the oxide voltage drop and is given by

$$V_{ox} = V_g - V_{FB} - V_{semi} - V_{poly}$$

4.1.1. Local electron tunneling current $J_{nl}(t)$

The local area electron tunneling current density J_{nl} is given by [28]

$$J_{nl}(t) = AE_{cl}^2(t)T_{nl}(t) \tag{18}$$

where T_{nl} is the electron tunneling probability in the local area and using the WKB formula T_{nl} is given by

$$T_{nl} = \exp\left[-2\int_0^{x_t} k(x)\mathrm{d}x\right] \tag{19}$$

where x_t is the tunneling distance and $k(x)$ is the wave factor within the oxide. $k(x)$ is given by

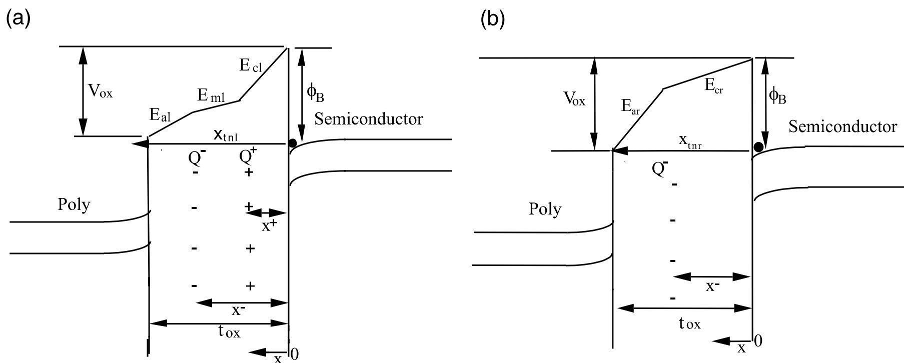

Fig. 5. (a) Energy band diagram of a MOS with trapped positive sheet charge Q^+ and negative sheet charge Q^- at their respective centroids in the local area. (b) Energy band diagram of a MOS with trapped negative sheet charge Q^- at its centroid in the robust area.

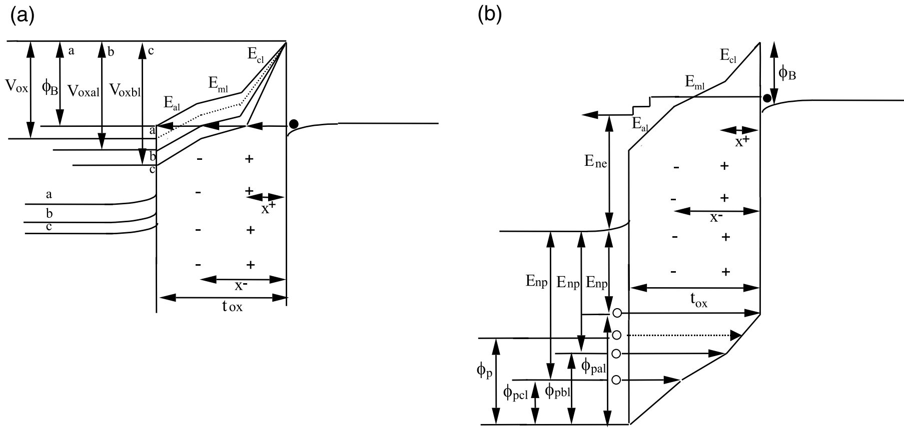

Fig. 6. (a) Energy band diagram showing corner oxide voltages Φ_B, V_{oxal}, V_{oxbl} corresponding to different electron tunneling distance t_{ox}, x^-, x^+ in the local area. (b) Energy band diagram showing corner barrier heights for hole Φ_{pal}, Φ_{pbl}, Φ_{pcl} corresponding to different hole tunneling distance t_{ox}, $t_{ox} - x^+$, $t_{ox} - x^-$ in the local area.

$$k(x) = \left[\frac{2m_{oxn}q}{\hbar^2}\Phi(x)\right]^{1/2}$$

$\Phi(x)$ is the variation of the potential with distance x and m_{oxn} is the electron effective mass.

Referring to Fig. 5(a) and using Eq. (19), the expression for the tunneling probability T_{nl} for electron with a tunneling distance x_{tnl} in general can be written as,

$$T_{nl} = T_{nl1}T_{nl2}T_{nl3}$$

where $T_{nl1} = \exp[-2(T_{n1})]$, $T_{nl2} = \exp[-2(T_{n2})]$, $T_{nl3} = \exp[-2(T_{n3})]$. The expression of T_{n1}, T_{n2}, T_{n3} can be obtained from the integral part of Eq. (19) using the proper expression of $k(x)$ along with appropriate boundary conditions for different regions inside the oxide and are given by

$$T_{n1} = \frac{2K_n}{3E_{cl}}\left[\Phi_B^{3/2} - (\Phi_B - E_{cl}x^+)^{3/2}\right] \tag{20a}$$

$$T_{n2} = \frac{2K_n}{3E_{ml}}\left[(\Phi_B - E_{cl}x^+)^{3/2} - \{\Phi_B - E_{cl}x^+ + E_{ml}(x^+ - x^-)\}^{3/2}\right] \tag{20b}$$

$$T_{n3} = \frac{2K_n}{3E_{al}}\left[\{\Phi_B - E_{cl}x^+ + E_{ml}(x^+ - x^-)\}^{3/2} - \{\Phi_B - E_{cl}x^+ + E_{ml}(x^+ - x^-) + E_{al}(x^- - x_{tnl})\}^{3/2}\right] \tag{20c}$$

where $K_n = \sqrt{2m_{oxn}q}/\hbar$.

For an applied fixed oxide voltage V_{ox} the tunneling condition will vary with time t as x_{tnl} changes with time t due to the time variation of Q^+ and Q^-. The variation of tunneling distance x_{tnl} with time t can be transformed into oxide voltages V_{ox}. Accordingly, there will be three corner oxide voltages namely V_{oxal}, V_{oxbl} and Φ_B corresponding to $x_{tnl} = x^+$, x^- and t_{ox} which will vary with time.

4.1.1.1. Calculation of corner oxide voltages V_{oxal}, V_{oxbl}. Referring to Fig. 6(a) and equating the corresponding expression of electron tunneling distance x_{tnl} at x^- and x^+, we obtain the corner oxide voltages V_{oxal}, V_{oxbl}. For $x^- < x_{tnl} < t_{ox}$ the expression of tunneling distance x_{tnl} is given by

$$x_{tnl} = x^- + \frac{\Phi_B - E_{cl}x^+ - E_{ml}(x^- - x^+)}{E_{al}} \tag{21}$$

and the corresponding oxide voltage V_{oxal} at $x_{tnl} = x^-$ is given by

$$V_{oxal} = V_m + \frac{t_{ox}}{x^-}\left[\Phi_B + \frac{Q^+(x^- - x^+)}{\varepsilon_{ox}}\right] \tag{22}$$

where

$$V_m = \frac{Q^+}{\varepsilon_{ox}}(x^+ - t_{ox}) - \frac{Q^-}{\varepsilon_{ox}}(x^- - t_{ox}) \tag{23}$$

For $x^+ < x_{tnl} < x^-$ the expression of tunneling distance is given by

$$x_{tnl} = x^+ + \frac{\Phi_B - E_{cl}x^+}{E_{ml}} \tag{24}$$

and the corresponding oxide voltage V_{oxbl} at $x_{tnl} = x^+$ is given by

$$V_{oxbl} = V_m + \frac{\Phi_B t_{ox}}{x^+} \tag{25}$$

The tunneling distance x_{tnl} and hence the corner voltages V_{oxal}, V_{oxbl} will change with applied voltage and time. Though the applied oxide voltage V_{ox} is invariant

with time, the tunneling condition for a fixed oxide voltage V_{ox} will change with time t due to change of corner voltages with time.

Depending on the corner voltages Φ_B, V_{oxal}, V_{oxbl} there are four different possible cases for electron tunneling for a specific charge distribution within the oxide. Each case has a different tunneling condition and should be treated separately to calculate the tunneling probability T_{nl} [28]. In the following section the electron tunneling probability T_{nl} for four different cases will be evaluated. All the following four cases refer to Fig. 6(a).

Case 1: For $V_{ox} < \Phi_B$ (i.e. $x_{tnl} = t_{ox}$) the tunneling probability T_{nl} is obtained from the basic Eqs. (20a)–(20c) and is given by

$$T_{nl} = T_{nl1}T_{nl2}T_{nl3}$$

Case 2: For $\Phi_B < V_{ox} < V_{oxal}$ (i.e. $x^- < x_{tnl} < t_{ox}$) the tunneling probability T_{nl} is also obtained from the basic Eqs. (20a)–(20c) and is given by

$$T_{nl} = T_{nl1}T_{nl2}T_{nl3}$$

where x_{tnl} in Eq. (20c) is given by Eq. (21).

Case 3: For $V_{oxal} < V_{ox} < V_{oxbl}$ (i.e. $x^+ < x_{tnl} < x^-$) the tunneling probability T_{nl} is obtained from the basic Eqs. (20a) and (20b) and is given by

$$T_{nl} = T_{nl1}T_{nl2'}$$

where

$$T_{nl2'} = \exp\left[-2\left(T_{n2'}\right)\right]$$

$T_{n2'}$ is obtained from Eq. (20b) by substituting x^- with x_{tnl} where x_{tnl} is given by Eq. (24).

Case 4: For $V_{ox} > V_{oxbl}$ (i.e. $0 < x_{tnl} < x^+$) the tunneling probability T_{nl} for this case is obtained from the basic Eq. (20a) and is given by

$$T_{nl} = T_{nl1'}$$

where

$$T_{nl1'} = \exp\left[-2\left(T_{n1'}\right)\right]$$

$T_{n1'}$ is obtained from Eq. (20a) by substituting x^+ with x_{tnl}, where

$$x_{tnl} = \frac{\Phi_B}{E_{cl}} \tag{26}$$

4.1.2. Local hole tunneling current $J_{pl}(t)$

From the anode hole injection model the hole tunneling current density J_{pl} is given by

$$J_{pl}(t) = \alpha_p J_{nl}(t)\gamma T_{pl} \tag{27}$$

where T_{pl} is the tunneling probability for holes in local area and will be different for different hole barrier heights.

4.1.2.1. Calculation of corner hole barrier heights Φ_{pal}, Φ_{pbl}, Φ_{pcl}.

Referring to Fig. 6(b) there will be three corner barrier heights for hot hole tunneling into the oxide from the anode corresponding to three different tunneling conditions. The barrier heights corresponding to hole tunneling distance $x_{tpl} = t_{ox}, x^+, x^-$ is denoted as Φ_{pal}, Φ_{pbl}, Φ_{pcl}, where

$$\Phi_{pal} = E_{cl}x^+ + E_{al}(t_{ox} - x^-) + E_{ml}(x^- - x^+) \quad \text{when} \quad x_{tpl} = t_{ox} \tag{28a}$$

$$\Phi_{pbl} = E_{al}(t_{ox} - x^-) + E_{ml}(x^- - x^+) \quad \text{when} \quad x_{tpl} = t_{ox} - x^+ \tag{28b}$$

$$\Phi_{pcl} = E_{al}(t_{ox} - x^-) \quad \text{when} \quad x_{tpl} = t_{ox} - x^- \tag{28c}$$

The analysis of T_{pl} will be similar to T_{nl}. Accordingly, the hole tunneling probability T_{pl} for four different cases will be calculated as follows. All the following four cases refer to Fig. 6(b).

Case 1: For $\Phi_p > \Phi_{pal}$ (i.e. $x_{tpl} = t_{ox}$) the hole tunneling probability T_{pl} is given by

$$T_{pl} = T_{pl1}T_{pl2}T_{pl3}$$

where, $T_{pl1} = \exp[-2(T_{p1})]$, $T_{pl2} = \exp[-2(T_{p2})]$, $T_{pl3} = \exp[-2(T_{p3})]$.

The expression of T_{p1}, T_{p2}, T_{p3} is similar to T_{n1}, T_{n2}, T_{n3} and can be obtained from the basic equations (20a)–(20c) by replacing K_n, Φ_B, E_{cl}, E_{al}, x^+, x^-, x_{tnl} by K_p, Φ_p, E_{al}, E_{cl}, $t_{ox} - x^-$, $t_{ox} - x^+$, x_{tpl} respectively, where

$$K_p = \frac{\sqrt{2m_{oxp}q}}{\hbar}$$

Case 2: For $\Phi_{pbl} < \Phi_p < \Phi_{pal}$ (i.e. $t_{ox} - x^+ < x_{tpl} < t_{ox}$) the hole tunneling probability T_{pl} is similar to case 1 but with a different x_{tpl} value and is given by

$$T_{pl} = T_{pl1}T_{pl2}T_{pl3}$$

where

$$x_{tpl} = (t_{ox} - x^+) + \frac{\Phi_p - E_{al}(t_{ox} - x^-) - E_{ml}(x^- - x^+)}{E_{cl}} \tag{29}$$

Case 3: For $\Phi_{pcl} < \Phi_p < \Phi_{pbl}$ (i.e. $t_{ox} - x^- < x_{tpl} < t_{ox} - x^+$) the hole tunneling probability T_{pl} is given by

$$T_{pl} = T_{pl1}T_{pl2'}$$

where

$$T_{pl2'} = \exp[-2(T_{p2'})]$$

$T_{p2'}$ can be obtained from Eq. (20b) by replacing K_n, Φ_B, E_{cl}, x^+, x^- by K_p, Φ_p, E_{al}, $t_{ox} - x^-$, x_{tpl} respectively, where

$$x_{\mathrm{tpl}} = (t_{\mathrm{ox}} - x^-) + \frac{\Phi_{\mathrm{p}} - E_{\mathrm{al}}(t_{\mathrm{ox}} - x^-)}{E_{\mathrm{ml}}} \tag{30}$$

Case 4: For $\Phi_{\mathrm{p}} < \Phi_{\mathrm{pcl}}$ (i.e. $0 < x_{\mathrm{tpl}} < t_{\mathrm{ox}} - x^-$) the hole tunneling probability T_{pl} is given by

$$T_{\mathrm{pl}} = T_{\mathrm{pl1'}}$$

where

$$T_{\mathrm{pl1'}} = \exp[-2(T_{\mathrm{p1'}})]$$

$T_{\mathrm{p1'}}$ can be obtained from Eq. (20a) by substituting K_{n}, Φ_{B}, E_{cl}, x^+ by K_{p}, Φ_{p}, E_{al}, x_{tpl} respectively, where

$$x_{\mathrm{tpl}} = \frac{\Phi_{\mathrm{p}}}{E_{\mathrm{al}}} \tag{31}$$

4.2. Robust area currents $J_{nr}(t)$ and $J_{pr}(t)$

The analysis of robust area current density $J_{\mathrm{nr}}(t)$ and $J_{\mathrm{pr}}(t)$ is exactly similar to the corresponding local area current density $J_{\mathrm{nl}}(t)$ and $J_{\mathrm{pl}}(t)$. The expression for the cathode field E_{cr} and anode field E_{ar} in the robust area can be obtained from Eqs. (17a)–(17c) by setting $Q^+ = 0$. Accordingly, there are three different cases for the robust area currents $J_{\mathrm{nr}}(t)$ and $J_{\mathrm{pr}}(t)$. Referring to Fig. 5(b) the distribution of electric field in the robust area is given by

$$E_{\mathrm{cr}} = \frac{1}{t_{\mathrm{ox}}}\left[V_{\mathrm{ox}} + \frac{Q^-}{\varepsilon_{\mathrm{ox}}}(x^- - t_{\mathrm{ox}})\right] \tag{32a}$$

$$E_{\mathrm{ar}} = E_{\mathrm{cr}} + \frac{Q^-}{\varepsilon_{\mathrm{ox}}} \tag{32b}$$

4.2.1. Robust electron tunneling current J_{nr}

The robust area electron tunneling current density J_{nr} is given by

$$J_{\mathrm{nr}}(t) = AE_{\mathrm{cr}}^2(t)T_{\mathrm{nr}}(t) \tag{33}$$

where T_{nr} is the electron tunneling probability in the robust area. Similar to T_{nl}, there will be three different cases for T_{nr} depending on the electron tunneling distance x_{tnr} in robust area. Referring to Fig. 7(a) these three cases are

Case 1: $V_{\mathrm{ox}} < \Phi_{\mathrm{B}}$ (i.e. $x_{\mathrm{tnr}} = t_{\mathrm{ox}}$),

Case 2: $\Phi_{\mathrm{B}} < V_{\mathrm{ox}} < V_{\mathrm{oxar}}$ (i.e. $x^- < x_{\mathrm{tnr}} < t_{\mathrm{ox}}$),

Case 3: $V_{\mathrm{ox}} > V_{\mathrm{oxar}}$ (i.e. $0 < x_{\mathrm{tnr}} < x^-$) where the expression for V_{oxar} is given by

$$V_{\mathrm{oxar}} = \frac{t_{\mathrm{ox}}\Phi_{\mathrm{B}}}{x^-} - \frac{Q^-(x^- - t_{\mathrm{ox}})}{\varepsilon_{\mathrm{ox}}} \tag{34}$$

Following the same procedure as described in Section 4.1.1 for T_{nl}, the tunneling probability T_{nr} for these three different cases can be similarly evaluated.

4.2.2. Robust hole tunneling current J_{pr}

The hole tunneling current density in the robust area J_{pr} is similar to J_{pl} and is given by

$$J_{\mathrm{pr}} = \alpha_{\mathrm{p}} J_{\mathrm{nr}} \gamma T_{\mathrm{pr}} \tag{35}$$

where T_{pr} is the hole tunneling probability in the robust area. Similar to T_{pl}, there will be three different cases for T_{pr} depending on the hole barrier heights (i.e. hole tunneling distance x_{tpr}) in robust area. Referring to Fig. 7(b) these three cases are

Case 1: $\Phi_{\mathrm{p}} > \Phi_{\mathrm{par}}$ (i.e. $x_{\mathrm{tpr}} = t_{\mathrm{ox}}$),

Case 2: $\Phi_{\mathrm{pbr}} < \Phi_{\mathrm{p}} < \Phi_{\mathrm{par}}$ (i.e. $t_{\mathrm{ox}} - x^- < x_{\mathrm{tpr}} < t_{\mathrm{ox}}$),

Case 3: $\Phi_{\mathrm{p}} < \Phi_{\mathrm{pbr}}$ (i.e. $0 < x_{\mathrm{tpr}} < t_{\mathrm{ox}} - x^-$), where

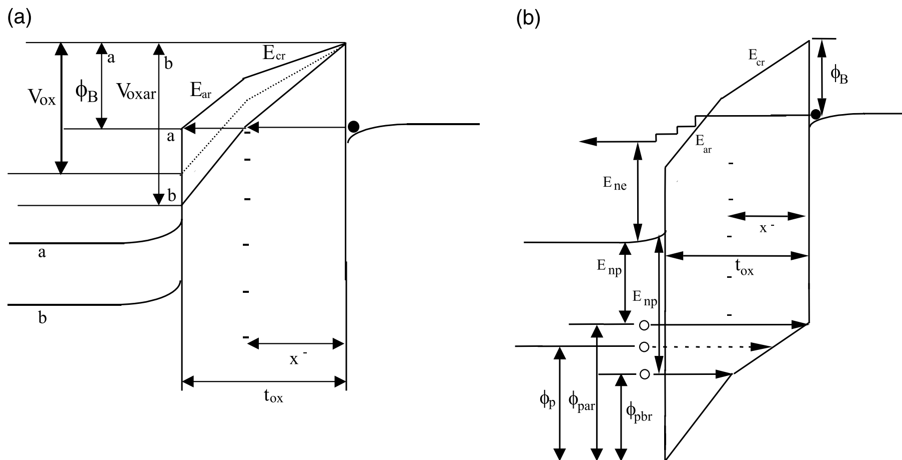

Fig. 7. (a) Energy band diagram showing corner oxide voltages Φ_{B}, V_{oxar} corresponding to different electron tunneling distance t_{ox}, x^- in the robust area. (b) Energy band diagram showing corner barrier heights for hole Φ_{par}, Φ_{pbr} corresponding to different hole tunneling distance t_{ox}, $t_{\mathrm{ox}} - x^-$ in the robust area.

$$\Phi_{\rm par} = E_{\rm ar}(t_{\rm ox} - x^-) + E_{\rm cr}x^-; \quad \text{when} \quad x_{\rm tpr} = t_{\rm ox} \tag{36a}$$

$$\Phi_{\rm pbr} = E_{\rm ar}(t_{\rm ox} - x^-) \quad \text{when} \quad x_{\rm tpr} = t_{\rm ox} - x^- \tag{36b}$$

Following the same procedure as described in Section 4.1.2 for $T_{\rm pl}$, the tunneling probability $T_{\rm pr}$ for these three different cases can be evaluated.

5. Calculation of Q^+ and Q^-

For relatively thicker oxides, the electron trapping is significant and the electron tunneling current tends to decrease due to it. However, for thinner oxides the effect of electron trapping is almost negligible. The electron tunneling current density $J_{\rm n}(t)$ decreases by more than an order of magnitude during the oxide lifetime due to significant electron trapping under constant voltage stress [20]. The variation of negative charge $Q^-(t)$ can be calculated using the first order electron trapping model [29] and is given by

$$Q^-(t) = qN_{\rm e}\left(1 - \exp\left(\int_0^t J_{\rm n}(t)\sigma_{\rm e}/q\right)\right) \tag{37}$$

where $N_{\rm e}$ is the preexisting trap density and $\sigma_{\rm e}$ is the capture cross-section for the existing traps. Most of the time the negative charge Q^- is calculated assuming $J_{\rm n}(t)$ as constant which is far from true for thicker oxides. The negative charge Q^- for thicker oxides can be more accurately calculated from the following equation

$$Q^-(t) = qN_{\rm e}(1 - \exp(-(J_{\rm nave}(t)t/q)\sigma_{\rm e}) \tag{38}$$

where $J_{\rm nave}$ is the log average of the initial electron current density $J_{\rm n}(0)$ and final electron current density $J_{\rm n}(t)$ and is given by

$$J_{\rm nave}(t) = 10^{[\log J_{\rm n}(0) + \log J_{\rm n}(t)]/2} \tag{39}$$

Similarly, the positive charge $Q^+(t)$ can be calculated

$$Q^+(t) = \eta J_{\rm pave}(t)t \tag{40}$$

where η is the hole trapping efficiency [2,4] and $J_{\rm pave}(t)$ is the log average of the initial hole current density $J_{\rm p}(0)$ and final hole current density $J_{\rm p}(t)$ and is given by

$$J_{\rm pave}(t) = 10^{[\log J_{\rm p}(0) + \log J_{\rm p}(t)]/2} \tag{41}$$

The total hole current density $J_{\rm p}(t)$ can be expressed in terms of $J_{\rm n}(t)$ after making some valid assumptions. From Eqs. (15), (16b), (27) and (35) $J_{\rm p}(t)$ is given by

$$J_{\rm p}(t) = \frac{\alpha_{\rm p}\gamma\{J_{\rm nl}(t)T_{\rm pl}A_{\rm l} + J_{\rm nr}(t)T_{\rm pr}A_{\rm r}\}}{A_{\rm l} + A_{\rm r}} \approx \frac{\alpha_{\rm p}\gamma\left\{J_{\rm nl}(t)\exp\left(-\frac{C}{E_{\rm al}}(\Phi_{\rm p})^{3/2}\right)A_{\rm l} + J_{\rm nr}(t)\exp\left(-\frac{C}{E_{\rm ar}}(\Phi_{\rm p})^{3/2}\right)A_{\rm r}\right\}}{A_{\rm l} + A_{\rm r}} \tag{42}$$

For the sake of simplicity we assume that the variation of anode field $E_{\rm al}$ and $E_{\rm ar}$ with time t is small and $E_{\rm al} \approx E_{\rm ar} \approx E_{\rm ox}$. Hence the expression of $J_{\rm p}(t)$ in terms of $J_{\rm n}(t)$ can be given by

$$J_{\rm p}(t) = \alpha_{\rm p}\gamma\left\{\exp\left(-\frac{C}{E_{\rm ox}}(\Phi_{\rm p})^{3/2}\right)\right\}J_{\rm n}(t) \tag{43}$$

The injected electron current density $J_{\rm n}(t)$ at $t = 0$ is given by

$$J_{\rm n}(0) = J_{\rm n} = AE_{\rm ox}^2\exp(-B/E_{\rm ox}) \tag{44}$$

where

$$B = \frac{8\pi}{3h}\sqrt{2m_{\rm oxn}q}\,\Phi_{\rm B}^{3/2} \tag{45}$$

A computer program is simulated to solve for $J_{\rm n}(t)$ numerically using our model equations. Once $J_{\rm n}(t)$ is determined $J_{\rm p}(t)$, $Q^+(t)$ and $Q^-(t)$ can be determined using Eqs. (38)–(43). The value of x^-, the centroid of negative charge Q^- is chosen $0.6t_{\rm ox}$ in our simulation. On the other hand x^+, the centroid of the positive charge Q^+ is an adjustable parameter and its value is chosen as $0.2t_{\rm ox}$. Values of both x^+ and x^- are consistent with the experimental finding as reported in the literature [1,2,29,30]. A value of 10^{-5} is chosen for η [2,4,15,31] and values of $N_{\rm e}$ and $\sigma_{\rm e}$ are taken from Ref. [29].

6. Results and discussion

In this section the $t_{\rm BD}$ and $Q_{\rm BD}$ results obtained from our model will be compared with the experimental one as extracted from Refs. [3,4,25]. The results for time dependence of $J_{\rm n}(t)$ and $J_{\rm p}(t)$ determined from our proposed anode hole injection model will also be discussed and be compared with experimental results taken from Ref. [20].

6.1. Q_{BD} results

Combining Eqs. (1), (14) and (15) the charge to breakdown $Q_{\rm BD}$ is calculated to predict the oxide lifetime of a $\rm n^+p$ MOS structure. The oxide voltage $V_{\rm ox}$ for a specific structure ($\rm n^+p$ or $\rm p^+n$) and gate bias polarity can be computed using Table 1. The maximum value of K' in the Table 1 is about 1.2 V as it corresponds to the maximum poly/Si band bending. The thickness dependence of $Q_{\rm p}$ in Eq. (1) is extracted from Ref. [3]. Hole effective mass $m_{\rm oxp}$ is a fitting parameter in Eq. (15) for computing hole generation efficiency $J_{\rm p}/J_{\rm n}$ and is chosen

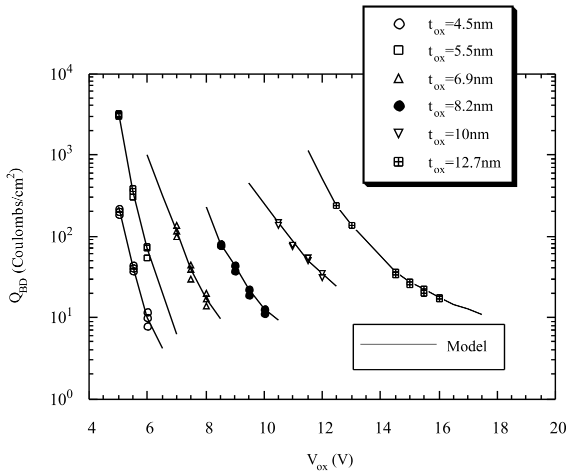

Fig. 8. Charge to breakdown (Q_{BD}) vs oxide voltage V_{ox} for thin oxides. The solid line represents the results obtained from our model and the corresponding markers represent the experimental data as extracted from Refs. [3,4,32(© 1994 IEEE)].

$0.235m_0$, where m_0 is the free electron mass. The chosen value of m_{oxp} used in our model lies within the range of the m_{oxp} values previously published in Refs. [20,25, 32,33]. Fig. 8 displays the simulated Q_{BD} results determined from our model and the corresponding experimental Q_{BD} data as a function of oxide voltage V_{ox} for a variety of oxide thickness. The results obtained from our model as shown in Fig. 8 demonstrates that there is very good agreement between our results and the experimental results previously published [3,4] in the literature for a wide range of oxide voltages. It is evident from Fig. 8 that the change in Q_{BD} behavior for thicker oxides is relatively flat in contrast to thinner oxides. This can be explained on the basis of Fig. 6(a) (E_{ne} vs V_{ox}) and Fig. 6(b) (γ vs V_{ox}). Both E_{ne} and γ increases with V_{ox}. From Eq. (13) it is shown that increase of E_{ne} tends to decrease ϕ_p whereas increase in γ increases ϕ_p. However, the effect of E_{ne} is more dominant on ϕ_p than γ. In thinner oxides, the electron travels through the oxide almost ballistically and the energy gained by an electron E_{ne} changes very rapidly with the change of oxide voltage V_{ox} whereas the corresponding change in thicker oxides is very small.

6.2. $J_n(t)$ and $J_p(t)$ results

Fig. 9(a) and (b) shows the variation of J_n and J_p with time t of a 8.2 nm gate oxide for two different gate voltages. Electron effective mass m_{oxn} used in the calculation of $J_n(t)$ is extracted from the slope of J_n/E_{ox}^2 vs $1/E_{ox}$ plot for $t_{ox} = 8.2$ nm [19,34]. Currents J_n and J_p as a function of time can be measured using the carrier

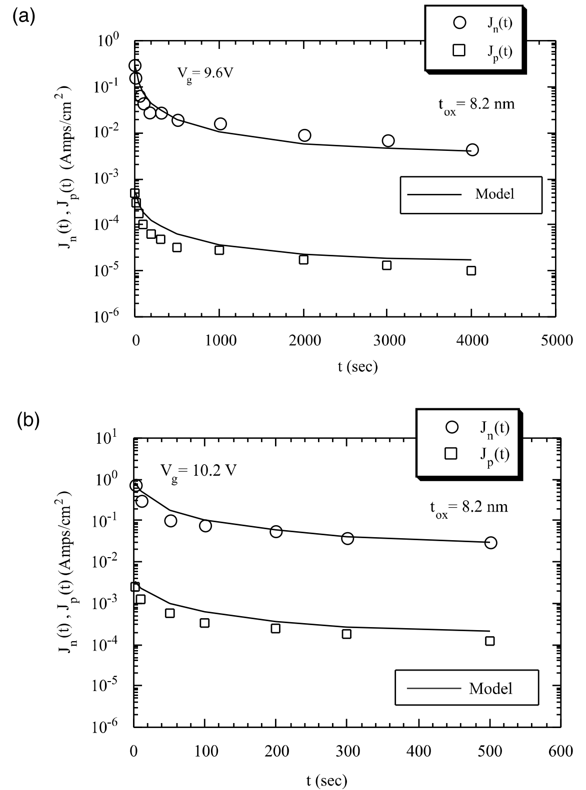

Fig. 9. (a) Time dependence of injected electron current density $J_n(t)$ and generated hole current density $J_p(t)$ for a constant voltage stress of 9.6 V of a 8.2 nm oxide. The solid line represents the results obtained from our model and the corresponding markers represent the experimental data [20](© 1994 IEEE). (b) Time dependence of injected electron current density $J_n(t)$ and generated hole current density $J_p(t)$ for a constant voltage stress of 10.2 V of a 8.2 nm oxide. The solid line represents the results obtained from our model and the corresponding markers represent the experimental data [20](© 1994 IEEE).

separation technique [3,20]. As shown in these figures the results from our model very closely follows the experimental data. The total tunneling current $J_n(t)$ will depend on $J_{nl}(t)$, $J_{nr}(t)$ and A_l/A_r. As the ratio of A_l to A_r is very small ($\approx 10^{-6}$) the total tunneling current $J_n(t)$ prior to the breakdown (buildup stage) will be dominated by $J_{nr}(t)$. Due to significant electron trapping in the robust area, $J_{nr}(t)$ will decrease with time t and hence also $J_n(t)$ before the breakdown occurs. Similarly, the hole tunneling current $J_p(t)$ will be strongly dependent on $J_{pr}(t)$ which again depends on $J_{nr}(t)$ and $T_{pr}(t)$ as given by Eq. (35). But the variation of $T_{pr}(t)$ with time t is less significant and hence $J_{pr}(t)$ varies mainly with $J_{nr}(t)$. The exponential variation of $J_n(t)$ and hence $J_p(t)$ is mainly due to the exponential behavior of $Q^-(t)$ with time t as given by Eq. (38).

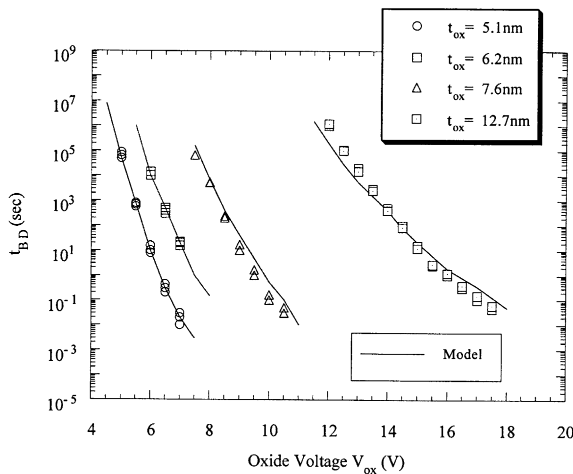

Fig. 10. Time to breakdown t_{BD} vs oxide voltage V_{ox} for thin oxides. The solid line represents the results obtained from our model and the corresponding markers represent the experimental data as extracted from Refs. [3,25](© 1993 IEEE).

6.3. t_{BD} results

Fig. 10 shows the simulated and experimental t_{BD} results as a function of oxide voltage for different oxide thickness. As shown in the Fig. 10 there is an excellent agreement between t_{BD} data obtained from our model and the experimental results. For thinner oxides, the effect of electron trapping is not significant and can be neglected. So, once Q_{BD} for thinner oxides is obtained as described in Section 6.1, t_{BD} for these oxides can be obtained using the expression $t_{BD} = Q_{BD}/J_n(2)$. However for relatively thicker oxides, the electron trapping effect cannot be neglected and the stressing tunneling current density $J_n(t)$ decreases significantly with stress time as shown in Fig. 9(a) and (b) and hence prolongs the breakdown time [25]. Hence, t_{BD} for this oxides can only be obtained by using $t_{BD} = Q_{BD}/J_{nave}(t_{BD})$. Current $J_{nave}(t_{BD})$ can be obtained from Eq. (39) with proper value of Q^+ and Q^- substituted in the relevant equations. According to the hole induced breakdown mechanism the positive charge Q^+ reaches a critical value $Q_{ot} = \eta Q_p$ [2,4] at breakdown while the negative charge Q^- prior to the breakdown can be approximately obtained from Eq. (38) by replacing t with $\tau_0 \exp(G/E_{ox})$ [35].

7. Conclusions

A comprehensive model is proposed for describing the charge buildup stage during the oxide breakdown process for thin oxides. The model is based on hole injection from the anode and is capable of determining the time dependence of injected electron current density J_n and generated hole current density J_p. The latter quantity is then used to evaluate the buildup of the positive charge with stress time due to hole trapping. It is shown that though the brief runway stage of the oxide breakdown process is determined by the enhancement of the cathode field in the local area due to hole trapping, the long buildup stage of the oxide breakdown process is determined by electron trapping in the robust area. A model is also presented in this paper to predict satisfactorily the charge to breakdown Q_{BD} and time to breakdown t_{BD} of thin oxides for a wide range of oxide voltages. Several important effects such as poly-depletion, quantum yield, trapping kinetics and different tunneling conditions are carefully considered while developing the model.

References

[1] Holland S, Chen IC, Ma TP, Hu C. IEEE Electron Dev Lett 1984;EDL-5:302.
[2] Chen IC, Holland SE, Hu C. IEEE Trans Electron Dev 1985;32:413.
[3] Schuegraf KF, Hu C. Semicond Sci Technol 1994;9:989.
[4] Chen IC, Holland S, Hu C. IEDM Tech Dig 1986:660.
[5] Chen IC, Holland S, Young KK, Chang C, Hu C. Appl Phys Lett 1986;49:669.
[6] Fischetti MV, Weinberg ZA, Calise JA. J Appl Phys 1985;57:418.
[7] Lee KH, Campbell SA. J Appl Phys 1993;73:4434.
[8] Kim JH, Sanchez JJ, DeMassa TA, Quddus MT, Smith D, Shaapur F, Weiss K, Liu CH. J Appl Phys 1998;84:1430.
[9] Hemink G, Endoh T, Shirota R. Jpn J Appl Phys 1994;33:546.
[10] Lu Y, Sah CT. J Appl Phys 1994;76:4724.
[11] Gao X, Yee SS. J Appl Phys 1994;76:5795.
[12] Satake H, Toriumi A. IEDM Tech Dig 1993:337.
[13] Weinberg ZA, Fischetti MV. J Appl Phys 1985;57:443.
[14] Weinberg ZA, Fischetti MV. J Appl Phys 1986;59:824.
[15] Holland S, Chen IC, Hu C. IEEE Electron Dev Lett 1987;EDL-8:572.
[16] Lee SW, Liang C, Pan CS, Lin W, Mark JB. IEEE Electron Dev Lett 1992;2–4.
[17] Schuegraf KF, King CC, Hu C. International Symposium on VLSI Technology, systems, and applications, 1993:86.
[18] Quddus MT, DeMassa TA, Sanchez JJ. IEEE Proceedings of 13th Biennial UGIM Microelectronics Symposium, 1999:123.
[19] Quddus MT, DeMassa TA, Sanchez JJ. J Microelectron Engng 2000;51–52:357.
[20] Schuegraf KF, Hu C. IEEE Trans Electron Dev 1994;41:761.
[21] Arora ND, Rios R, Huang CL. IEEE Trans Electron Dev 1995;42:935.
[22] Quddus MT. PhD dissertation, Dept of Elec Engng Arizona State University, 1999. p. 63.
[23] Chang C, Hu C, Brodersen RW. J Appl Phys 1985;57: 302.

[24] Dimaria DJ, Cartier E, Buchanan DA. J Appl Phys 1996;80:304.
[25] Schuegraf KF, Hu C. IEEE/IRPS 1993;7.
[26] Kobayashi K, Teramoto A, Hirayama M, Fujita Y. J Appl Phys 1995;77:3277.
[27] Thompson SE, Nishida T. J Appl Phys 1992;72:4683.
[28] Wu C-Y, Chen C-F. IEEE Trans Electron Dev 1987;34:1590.
[29] Liang MS, Hu C. IEDM Tech Dig 1981:396.
[30] Chen IC, Holland S, Hu C. IEEE Electron Dev Lett 1986;7:164.
[31] Chen IC, Holland S, Hu C. IEEE/IRPS 1985;24.
[32] Schuegraf KF, Hu C. IEEE/IRPS 1994;126.
[33] Eitan B, Kolodny A. Appl Phys Lett 1983;43:106.
[34] Weinberg ZA. J Appl Phys 1982;53:5052.
[35] Moazzami R, Lee J, Chen IC, Hu C. IEDM 1988;710.